Earthquakes Drive Focused Denudation along a Tectonically Active Mountain Front

Gen Li[1*], A. Joshua West[1], Alexander L. Densmore[2], Zhangdong Jin[3], Fei Zhang[3], Jin Wang[3], Marin Clark[4], and Robert G. Hilton[2]

[1]Department of Earth Sciences, University of Southern California, Los Angeles, CA 90089, USA
[2]Institute of Hazard, Risk and Resilience and Department of Geography, Durham University, Durham DH1 3LE, UK
[3]State Key Laboratory of Loess and Quaternary Geology, Institute of Earth Environment, Chinese Academy of Sciences, Xi'an 710075, China
[4]Department of Earth and Environmental Sciences, University of Michigan, Ann Arbor, MI 48109, USA

[*]corresponding author
Phone: +1-(213)740-5825
Email: genli@usc.edu

Manuscript in revision for *Earth and Planetary Science Letters*

Abstract

Earthquakes cause widespread landslides that can increase erosional fluxes observed over years to decades. However, the impact of earthquakes on denudation over the longer timescales relevant to orogenic evolution remains elusive. Here we assess erosion associated with earthquake-triggered landslides in the Longmen Shan range at the eastern margin of the Tibetan Plateau. We use the M_w 7.9 2008 Wenchuan and M_w 6.6 2013 Lushan earthquakes to evaluate how seismicity contributes to the erosional budget from short timescales (annual to decadal, as recorded by sediment fluxes) to long timescales (kyr to Myr, from cosmogenic nuclides and low temperature thermochronology). Over this wide range of timescales, the highest rates of denudation in the Longmen Shan coincide spatially with the region of most intense landsliding during the Wenchuan earthquake. Across sixteen gauged river catchments, sediment flux-derived denudation rates following the Wenchuan earthquake are closely correlated with seismic ground motion and the associated volume of Wenchuan-triggered landslides ($r^2 > 0.6$), and to a lesser extent with the frequency of high intensity runoff events ($r^2 = 0.36$). To assess whether earthquake-induced landsliding can contribute importantly to denudation over longer timescales, we model the total volume of landslides triggered by earthquakes of various magnitudes over multiple earthquake cycles. We combine models that predict the volumes of landslides triggered by earthquakes, calibrated against the Wenchuan and Lushan events, with an earthquake magnitude-frequency distribution. The long-term, landslide-sustained "seismic erosion rate" is similar in magnitude to regional long-term denudation rates (~0.5-1 mm yr^{-1}). The similar magnitude and spatial coincidence suggest that earthquake-triggered landslides are a primary mechanism of long-term denudation in the frontal Longmen Shan. We propose that the location and intensity of seismogenic faulting can contribute to focused denudation along a high-relief plateau margin.

1. Introduction

Mountain erosion affects rates and patterns of crustal deformation including seismogenic faulting [e.g., Steer et al., 2014] and flexural-isostatic responses [e.g., Molnar and England, 1990], and influences the geological carbon cycle and consequently the climate system [e.g., Raymo et al., 1988; Wang et al., 2016]. Large earthquakes are thought to play an important role in the denudation of tectonically-active mountain ranges because they cause widespread landslides that generate large volumes of clastic sediment [Keefer, 1994; Larsen et al., 2010; Hovius et al., 2011; Parker et al., 2011; Wang et al., 2015a]. Delivery of landslide debris to rivers and the subsequent fluvial evacuation can increase erosion rates over years to decades [e.g., Hovius et al., 2011; Wang et al., 2015a]. However, over longer timescales relevant to orogenic evolution (10^4-10^6 yr), the role of earthquakes in denudation remains less well constrained, even though the volume of seismically triggered landslides may be sufficient to partly or wholly counteract seismically induced rock uplift [Parker et al., 2011; Hovius et al., 2011; Li et al., 2014; Marc et al., 2016a].

Detailed mapping of landslides [e.g., Keefer, 1994; Parker et al., 2011; Li et al., 2014; Xu et al., 2015] and hydrological gauging of sediment fluxes [e.g., Hovius et al., 2011; Wang et al., 2015a] capture the aftermath of individual events. Across multiple events, landslide volume scales with earthquake magnitude [Keefer, 1994; Malamud et al., 2004; Marc et al., 2016b]. Combined with return time statistics for earthquakes, this scaling relationship can yield an estimate of long-term landslide rate that should reflect a "seismic erosion rate" associated with repeated earthquakes, assuming fluvial evacuation of landslide debris [Keefer, 1994; Malamud et al., 2004; Lavé and Burbank, 2004; Li et al., 2014; Marc et al., 2016a]. Keefer (1994) found that seismic erosion rates are comparable to fluvial sediment yields measured in several regions. Cosmogenic nuclide and thermochronology datasets allow us to expand this approach to consider denudation rates measured over longer timescales that encompass multiple earthquakes and that are more relevant to mountain belt evolution. In this study, we focus on the Longmen Shan region of central China, where the 2008 M_w 7.9 Wenchuan and 2013 M_w 6.6 Lushan earthquakes allow us to make estimates of seismic erosion rates. We evaluate both the spatial distribution and magnitude of these rates in the context of datasets from fluvial sediment fluxes, cosmogenic nuclides, and low-temperature thermochronology [e.g., Kirby et al., 2002; Ouimet et al., 2009; Godard et al., 2010; Liu-Zeng et al., 2011; Wang et al., 2015a].

The steep Longmen Shan mountain range defines the eastern margin of the Tibetan Plateau. This region has been at the nexus of contentious debates over the importance of motion along shallow faults versus ductile flow of lower crust for collisional mountain building [e.g., Clark and Royden, 2000; Hubbard and Shaw, 2009]. Focused denudation along the steep topographic front of such plateau margins may exert an important influence on deformation [e.g., Beaumont et al., 2001]. However, the relative roles of tectonic and climatic drivers of denudation – and thus the link

between climate and the geodynamic processes – remain unresolved, both for the Longmen Shan [e.g., Ouimet et al., 2009; Godard et al., 2010; Liu-Zeng et al., 2011] and elsewhere. We aim to gain new general insight into the long-term role of seismic erosion in tectonically active mountains and how it may contribute to focused denudation along the eastern margin of the Tibetan plateau.

2. Setting

With elevations rising to higher than 5 km over a 50 km horizontal distance, the eastern Longmen Shan flank represents one of Earth's steepest plateau margins [Clark and Royden, 2000; Densmore et al., 2007; Burchfiel et al., 2008]. Several Yangtze headwater rivers (mainly the Min Jiang, Fu Jiang, Tuo Jiang, Qingyi Jiang and Dadu He) drain from the Longmen Shan into the Sichuan Basin (Figure 1a). A series of dextral-thrusting, oblique-slip faults bound the mountain front and comprise the Longmen Shan fault system [Densmore et al., 2007; Burchfiel et al., 2008]. The bedrock geology consists mainly of Proterozoic basement granitoids and high-grade metamorphic rocks, metamorphosed sedimentary rocks of a Paleozoic passive margin sequence, unmetamorphosed sedimentary rocks associated with a Mesozoic foreland-basin succession, and limited Cenozoic sediments [Burchfiel et al., 2008]. Climatically, the Longmen Shan range is located at the transition between the domains dominated by the east Asian monsoon and the westerlies. Across the Longmen Shan, average annual rainfall decreases from the margin (~1100 mm yr^{-1}) towards the plateau (as low as ~ 600 mm yr^{-1}) [Liu-Zeng et al., 2011]. This regional climate pattern is largely determined by the high topography, which acts as an orographic barrier and may also affect atmospheric circulation by heating of the atmosphere [Molnar et al., 2010 and references therein]. Precipitation is highly seasonal, with most rainfall during the wet season from June to September.

The M_w 7.9 Wenchuan earthquake on May 12th, 2008 initiated in the southern Longmen Shan, near the town of Yingxiu, and ruptured northeastward for ~270 km along the Longmen Shan fault system (Figure 1a) [Burchfiel et al., 2008; Shen et al., 2009]. The strong ground motion triggered > 56,000 landslides in the steep mountainous topography (Figure 1a) [Parker et al., 2011; Li et al., 2014; Xu et al., 2014]. These seismically induced landslides introduced large volumes of clastic sediment into the fluvial system, estimated to total ~3 km^3 [Li et al., 2014]. Prior work has aimed to understand the effects on sediment transport. Li et al. (2014) documented the spatial pattern and volume of landsliding, and Li et al. (2016) assessed the connectivity of these landslides to the river network as a means of understanding their behavior as sediment sources. Wang et al. (2015a) used data from the Chinese Hydrology Bureau to quantify suspended sediment transport rates. After the Wenchuan earthquake (2008-2012), suspended sediment fluxes from the Min Jiang, Fu Jiang and Tuo Jiang catchments increased by 3 to 7 times compared to pre-earthquake levels (2006-2007). Based on ^{10}Be concentrations in quartz from Min Jiang riverbed sands, West et al. (2014) suggested that bedload transport rates had increased by a similar order of magnitude to those of suspended load. The present

study takes advantage of this prior work, including the landslide inventory and sediment fluxes, in order to compare spatial patterns of denudation across a range of timescales.

We use the M_w 6.6 Lushan event as an additional constraint on the magnitude of seismic erosion rates. The Lushan earthquake occurred on April 20th, 2013 in the southern Longmen Shan, 80 km south of the Wenchuan epicenter (Figure 1a). This event initiated on a ramp in the range-front blind thrust fault, in the footwall of the Wenchuan rupture [Wang et al., 2014]. As in the Wenchuan event, widespread landsliding occurred in the southern Longmen Shan range during the Lushan earthquake. Xu et al. (2015) reported more than 20,000 co-seismic landslides, with a total area of 18.88 km^2 and an estimated volume of 0.042 km^3 across the region of the Lushan earthquake.

3. Materials and Approaches

3.1. Landslide inventory

For the Wenchuan earthquake, co-seismic and immediately post-seismic landslides (within six months after the earthquake) were mapped by Li et al. (2014). Landslide volumes were calculated from empirical landslide area-volume scaling relations [e.g., Larsen et al., 2010]. We assume that mapped landslides mainly resulted from the Wenchuan mainshock because we find that aftershocks contributed <5% of the total seismic moment release across the Longmen Shan, based on the seismic catalog spanning over six months following the mainshock [CSN Catalog, 2015]. This finding is consistent with observations from other earthquakes that suggest most landslides occur during the main shock [e.g., Roback et al., 2017]. Additional volume associated with post-seismic (e.g., storm-triggered) landslides is likely to be on the order of a few percent of the total landslide volume [Li et al., 2016 and references therein].

For the landsides triggered by the Lushan earthquake, we refer to the landslide inventory compiled by Xu et al. (2015), who also used empirical scaling relationships reported in Larsen et al. (2010) to estimate volumes from a landslide map based on satellite imagery. Xu et al. (2015) mapped Lushan landslides using images collected from April – May 2013, around five years after the Wenchuan earthquake but immediately after the Lushan event. Also, there is not much overlap between the mapping extents and the intensive shaking zones for the Lushan and Wenchuan events [Li et al., 2014; Xu et al., 2015]. Thus we expect limited influence on the mapped Lushan landslides from the Wenchuan earthquake.

3.2. Geomorphic characterization

In evaluating the spatial patterns of denudation in the Wenchuan region, we focus on three main catchments (Min Jiang, Fu Jiang and Tuo Jiang), comprising sixteen sub-catchments as delineated by Li et al. (2016) (Figure 1b and Table S1). SRTM30 digital elevation model (DEM) data have incomplete coverage of the study region, so we used void-filled SRTM90 DEM data for topographic analysis [Jarvis et al., 2008].

Slopes were calculated using standard algorithms provided in the ArcGIS platform (Figure 1d). Although the derived slopes vary as a function of DEM resolution [e.g., Larsen et al., 2014], the biases are systematic (e.g., Figure S1) so we expect little influence on the relative trends between different catchments. Relief was determined as the ranges of elevations in 2.5 km-radius and 5 km-radius circular windows. We also calculated the volumetric density of landslides (m^3 km^{-2}, landslide volume per unit catchment area) within each studied catchment (Table S1) and along a swath profile A-A' (Figure 1f). We derived channel steepness indexes (k_{sn}, normalized to θ_{ref} = 0.45, cf. Ouimet et al., 2009; symbol notation listed in Table 1) using the Stream Profiler toolbox (http://www.geomorphtools.org). DEM cells with drainage area < 1 km^2 were excluded to remove colluvial landscapes [Li et al., 2016]. To characterize ground motion associated with the Wenchuan earthquake, we used gridded peak ground acceleration (PGA) data obtained from the USGS ShakeMap (USGS Hazard Program, http://earthquake.usgs.gov/earthquakes).

3.3. Hydrological data

Wang et al. (2015a) analyzed data from the Chinese Hydrology Bureau and calculated total suspended load fluxes and runoff from 16 gauging stations across the Longmen Shan catchments (Figure 1a). This data covered both the pre-Wenchuan (2006-2007) and the post-Wenchuan (2008-2012) time periods. Using this dataset, Li et al. (2016) derived the suspended load fluxes for sub-catchments, by taking the differences between fluxes gauged at one station and all neighboring upstream stations, following a mass balance principle [Li et al., 2016]. Three sub-catchments yielded negative sediment fluxes, attributed to large sedimentary sinks such as reservoirs. As in Li et al. (2016), these were excluded from analysis (catchments labeled as "N.A." in Figure 1b).

Based on the gauged discharge and catchment area, we derived annual runoff for sub-catchments using an analogous mass balance approach to that for calculating sediment fluxes. Wang et al. (2015a) suggested that high magnitude runoff events play an important role in post-Wenchuan suspended sediment transport. We explored different thresholds for high magnitude runoff and found that a 6 mm day^{-1} threshold best correlated with denudation rates (Figure S2 in Supporting Information), close to the 5 mm day^{-1} used by Wang et al. (2015a). We also calculated specific stream power (ω) adopting the approach of Burbank et al. (2003) (details in Supporting Information) using our compiled runoff and topography data.

3.4. Calculation of sediment flux-derived ("short term") denudation rates

The total mass flux from a river catchment (i.e., the denudation rate) includes suspended, bedload, and dissolved load. To calculate total denudation rates, we adopted the approach of Liu-Zeng et al. (2011), who determined a pre-Wenchuan earthquake ratio of dissolved load to suspended load of 19±6%, and a ratio of bedload to suspended load of 25±15%. After the earthquake (2009-2012), Jin et al. (2016) measured solute fluxes at two sites (Zhenjiangguan and Weizhou, Figure 1a) in the

Min Jiang catchment, yielding a post-earthquake dissolved:suspended load ratio of 19±7% (Table S3 and text in Supporting Information), similar to pre-earthquake estimates. Measurements of ^{10}Be concentrations in detrital quartz from bed sediments collected in 2009-2010 [West et al., 2014] indicate that, after the earthquake, bedload increased by a similar factor as suspended load. Thus the bedload:suspended load ratio is likely to be similar to that reported prior to the earthquake, i.e., 25±15%. Using these ratios between the dissolved load, bedload and suspended load, we calculated total denudation fluxes (t yr^{-1}) from the suspended sediment fluxes and converted these to denudation rates (mm yr^{-1}), assuming material density of 2.65×10^3 kg m^{-3} [cf. Liu-Zeng et al., 2011]. To account for low-relief, frontal plains, which are expected to contribute little to the denudation flux, we normalized the calculated denudation rates to the fraction of mountainous area (defined as areas > 800 m elevation) in each catchment (Figure 1b and Table S1). We have examined relationships between these denudation rates and various hydrological and topographic metrics we have calculated for the Longmen Shan (Section 3.2, 3.3).

3.5. Compilation of long-term (kyr to Myr) denudation rates

To characterize the denudation of the Longmen Shan over longer timescales, we compiled ^{10}Be-derived catchment-scale millennial denudation rates [Ouimet et al., 2009; Godard et al., 2010; Ansberque et al., 2015] and refer to a data set of bedrock cooling ages and corresponding exhumation rates across the mountain range from low-temperature thermochronology studies (apatite fission track (AFT), apatite (U-Th)/He (AHe), zircon fission track (ZFT) and zircon (U-Th)/He (ZHe)), compiled by Tian et al. (2013) [data from Arne et al., 1997; Kirby et al., 2002; Richardson et al., 2008; Godard et al., 2009; Wang et al., 2012; Tian et al., 2013]. Tian et al. (2013) converted the cooling ages to time-averaged exhumation rates assuming a one-dimensional, steady state upper crustal section and taking into account the effects of cooling rate on closure temperature together with heat advection during exhumation, following Reiners and Brandon (2006). For geothermal gradient, Tian et al. (2013) assumed a pre-exhumation geothermal gradient of 20 ℃ km^{-1}, which yields a syn-exhumation gradient of 23-30 ℃ km^{-1}, consistent with the present geothermal gradient in the Longmen Shan determined from thermal logging of local boreholes (> 4.5 km deep) and numerical modeling [Tian et al., 2013]. Uncertainties on the exhumation rates were propagated from uncertainties on thermochronology measurements [Tian et al., 2013].

3.6. Calculation of seismic erosion rate over multiple earthquake cycles

3.6.1. Approach to calculating seismic erosion rate

Over multiple recurrence cycles, earthquakes of various magnitudes occur at different frequency. To characterize the cumulative effect, we defined a seismic erosion rate (mm yr^{-1}) as the total volume of landslides triggered over multiple earthquake cycles and over a specified area, following Keefer (1994):

$$\dot{e} = \frac{\sum_{M_w} N(M_w) \times V_L(M_w)}{t \times A} \quad (1)$$

where t represents the total time (yr) over which repeated earthquakes are integrated, A is the area of the region of landslide occurrence, $N(M_w)$ is the number of landslide-triggering earthquakes in the magnitude bin [M_w, M_w+0.1], and $V_L(M_w)$ refers the corresponding landslide volume triggered by an earthquake of magnitude M_w.

Based on the Wenchuan landslide data, we assumed that all landslides have occurred within an intensive erosion zone along the frontal Longmen Shan (Section 4.1), with an area of 170 km ×80 km (A). This area, to first order, matches the areal extent of landslide occurrence predicted for a M_w 8 event by Keefer (1994), and the length of this region also approximates the rupture length of the Wenchuan earthquake [Burchfiel et al., 2008]. By distributing the total volume of earthquake-triggered landslides over area A and time period t, we obtain a spatially and temporally averaged rate of seismic erosion.

To calculate a seismic erosion rate from Eq. 1, we adopted a numerical integration approach (after Keefer, 1994; see details in Supporting Information). This approach combines (1) a scaling relationship between earthquake magnitude and the volume of earthquake-triggered landslides (Section 3.6.2) and (2) a statistical description of earthquake magnitude and corresponding frequency throughout an earthquake sequence (Section 3.6.3). Summing the landslide volumes throughout a full earthquake sequence, we determined the total volume of landslides occurring over a time period t that captures multiple earthquake cycles, yielding a long-term seismic erosion rate (Eq. 1).

3.6.2. Earthquake magnitude-landslide volume scaling relations: predictive models of the total volume of earthquake-triggered landslides

Descriptions of the landslide volume associated with earthquakes range from simple empirical regression of volume versus earthquake magnitude [e.g., Keefer, 1994; Malamud et al., 2004] to models that seek to capture the mechanics of landslide triggering, including slope stability as it relates to hillslope angles and near-surface rock strength [e.g., Gallen et al., 2015; Marc et al., 2016b]. Large uncertainties plague the empirical regressions, whereas the more mechanistic models – although able to reproduce global patterns [e.g., Marc et al., 2016b] – include parameters that are often not precisely known, for example those describing rock strength, earthquake asperity depth, and ground motion attenuation. To capture this range of approaches, we estimated seismic erosion rates using both empirical regression and the model of Marc et al. (2016b). We also calculated rates with a Longmen Shan-specific landslide volume model based on locally-calibrated parameters and ground motion equations. To most accurately estimate seismic erosion rates for the Longmen Shan region, we

evaluated the predictions of these different models with reference to the observed landslide volumes from the Wenchuan and Lushan cases (see Section 5.1). The global empirical regression model, global seismologically-based model, and Longmen Shan-specific model are summarized as follows.

Global empirical regression: Keefer (1994) and Malamud et al. (2004) compiled a global dataset of landslide inventories triggered by large earthquakes. They reported a logarithmic scaling relation between the total volume of landslides triggered by an earthquake, V_L, and earthquake magnitude, M_w [Malamud et al., 2004]:

$$\mathrm{Log}_{10}V_L = 1.42M_w - 11.26\ (\pm 0.52) \quad (2)$$

Global seismologically-based landslide model: Marc et al. (2016b) developed an approach to predict the total volume of earthquake-triggered landslides, taking into account seismogenic characteristics (e.g., seismic moment and asperity depth), landscape steepness, and material sensitivity (rock strength and pore pressure). We adopted this model using seismogenic and topographic parameters appropriate for the Wenchuan and Lushan earthquakes (see discussion in Section 4.3.1 and more details in Supporting Information).

Longmen Shan-specific landslide model: Using local observations of ground motion attenuation, we derived an earthquake magnitude-landslide volume scaling relation specific for the Longmen Shan (details in Supporting Information). In brief, we first defined a landslide volume-PGA relation using the Wenchuan data (following Meunier et al., 2007; Figure S3a in Supporting Information). We combined this with a locally-calibrated equation describing ground motion attenuation in the Longmen Shan and neighboring areas [Cui et al., 2012; Wang et al., 2015b; and references therein]:

$$\mathrm{Log}_{10}\mathrm{PGA} = c_1 + c_2M_w + c_3\mathrm{Log}_{10}(D + c_4) \quad (3)$$

where D represents distance to fault trace and c_1, c_2, c_3 and c_4 are empirical parameters, determined empirically from the Wenchuan data and other earthquakes in the Longmen Shan and neighboring region (see Figure S3b in Supporting Information). Combining the landslide volume-PGA relation and the PGA-M_w relation allows us to calculate the landslide volume for earthquakes across a range of earthquake magnitudes. The relation between earthquake magnitude and landslide volume can be well described by a logarithmic fit ($r^2 = 0.99$):

$$\mathrm{Log}_{10}V_L = 23.77\mathrm{Log}_{10}M_w - 11.91(\pm 0.07) \quad (4)$$

Slope angles also influence where landslides occur during earthquakes [Gallen et al., 2015; Marc et al., 2016b]. The Newmark model framework adopted by Gallen et al. (2015) accounts for slope angles but depends on assumptions about landslide

geometry, complicating its application in this case. However, consistent with studies of other earthquakes [Meunier et al., 2007], we find that in the case of the Longmen Shan PGA provides a good first-order empirical prediction of regional patterns in landslide occurrence without considering differences in slope angle (Figure S3a), perhaps because regional variability in slopes is relatively small when compared to PGA (Figure 1).

3.6.3. Longmen Shan earthquake sequence

Inferring a long-term seismic erosion rate from landslide volume predictions requires assumptions about the earthquake population over the timescales of multiple earthquake cycles. We simulated a sequence of earthquakes with various magnitudes using available seismological data from the Longmen Shan region. Because the Wenchuan earthquake ruptured almost the full length of the Longmen Shan frontal fault system [Burchfiel et al., 2008], M_w~8 represents a reasonable upper bound for earthquake magnitudes in the study area. We chose M_w~5 as a minimum magnitude for landslide triggering [Marc et al., 2016b]. The occurrence times of earthquakes of various magnitudes were determined using an earthquake frequency-magnitude distribution, with reference to regional historic seismicity data (China Earthquake Networks Center, 1657-2013) [Wang et al., 2015b] and results from paleoseismological and geodetic studies that suggest a recurrence interval (T) for Wenchuan-like events of 500 to 4000 years [Densmore et al., 2007; Shen et al., 2009; Thompson et al., 2015]. Across this range, the frequency-magnitude distribution of the Longmen Shan earthquakes could be well described using a truncated G-R function [Utsu, 1999 and references therein]. For the shortest estimated T (~500 years) [Thompson et al., 2015], Longmen Shan earthquake occurrence follows a classical, linear G-R relation.

To estimate seismic erosion rates following Eq. 1, we integrated predictions of the landslide volumes across the simulated earthquake sequences. Predicted landslide volumes are sensitive to the source depth of each simulated earthquake (see details in Supporting Information). For the global seismologically-based model [Marc et al., 2016b], we assumed a scaling relation between earthquake magnitude and focal depth, calibrated using the Wenchuan and the Lushan data. For the Longmen Shan-specific model, we used the scaling between earthquake magnitude and focal depth to define a characteristic landslide-triggering depth for each earthquake magnitude. We assumed that only earthquakes shallower than this depth cause landslides. For a given magnitude, we estimated the proportion of events with a focal depth shallower than this threshold based on a local seismic catalog [CSN Catalog, 2015; see Figure S4].

3.6.4. Failure and resetting of hillslopes over earthquake cycles

In using scaling relationships to calculate seismic erosion rate over multiple earthquake cycles, we have assumed that for each event there are sufficient hillslopes that are prone to fail. Following one earthquake cycle, failed hillslopes need to be re-weakened and re-steepened to initiate new landsliding in the following earthquake

cycle. We estimate that for the Longmen Shan, the pace of hillslope resetting is capable of keeping up with earthquake recurrence. For example, if we assume that the landscape fails following a patchwork fashion, then each earthquake triggers landslides on a different part of the unfailed landscape, allowing the failed hillslopes time to recover [e.g., Parker et al., 2015]. During the Wenchuan earthquake, around 1% of the high PGA-area (>0.2 g) was impacted by landsliding [Li et al., 2014]. Thus to fail the full landsliding-susceptible landscape would take ~100 earthquake cycles, or 50-400 kyrs (given an estimated return time of Wenchuan-like events of ~500-4000 yrs, see Section 3.6.3). If landscapes are steepened by river incision, the steepness resetting time (i.e., time required for resetting the failed landscape to pre-Wenchuan steepness) can be approximated as the ratio of the landslide depth versus the channel incision rate. We estimate an average steepness resetting time of ~6-26 kyr, or ~2-50 earthquake cycles for the Longmen Shan region (based on a mean Wenchuan landslide depth of ~6-13 m [Gallen et al., 2015] and a regional incision rate of ~0.5-1 mm yr^{-1} [Tian et al., 2015 and references therein]). This resetting time is much shorter than the 50-400 kyr to fully fail the landscape. Similarly, for a Longmen Shan chemical denudation rate of ~0.1-0.2 mm yr^{-1} [Liu-Zeng et al., 2011, and references therein] we anticipate that re-weakening of hillslope material to a depth of ~6-13 m would take 30-130 kyr. Therefore, regional channel incision and chemical weathering propagation rates should be fast enough to re-steepen and re-weaken failed landscapes, rejuvenating hillslopes for landsliding over multiple earthquake cycles.

4. Results and Discussion

4.1. Intensive and persistent denudation along the frontal Longmen Shan across timescales, and its relation to seismically triggered landsliding

4.1.1. Zone of focused denudation

Profiles of short-term denudation rates calculated from hydrological gauging and longer-term denudation rates from cosmogenic nuclides and thermochronology are shown in Figures 1 and 2, respectively. Rates are highest along the eastern Longmen Shan front and decrease towards the Tibetan Plateau along the A-A' trend. Based on these observations, we delineate an 80 km-wide zone of intensive erosion perpendicular to the strike of the mountain range (bounded by dashed blue lines in Figure 1c). This distinct zone features steep topography, maximum PGA, and the highest concentration of Wenchuan-triggered landslides (Figure 1c and Figure 1e). This region of intensive denudation was also identified by Liu-Zeng et al. (2011) based on denudation rates calculated from 1960s-1980s hydrological gauging data, though their rates were slightly higher (up to 0.5-0.8 mm yr^{-1}) than our pre-Wenchuan (2006-2007) estimates (0.24 ± 0.04 mm yr^{-1}). The difference is consistent with background declines in both water discharge and sediment flux in the Yangtze basin over the past 50 years, attributed in part to decreased precipitation as well as to human activities like dam building [Yang et al., 2015].

Long-term denudation rates (Section 3.5) along the A-A' trend (Figure 2a, b, c, d and e) are also higher (> 0.5 mm yr^{-1}) along the front of the eastern Longmen Shan,

compared to the western (plateau) side. The similarity to sediment flux-derived rates suggests a persistent denudation pattern across both modern and longer-term timescales. Both patterns are, to first order, similar to the distribution of the Wenchuan co-seismic landslides (Figure 2b, c, d and e). We suggest that seismicity associated with the Longmen Shan fault system, which runs along the front of the range, provides a mechanism for generating repeated landslides in this zone, as seen during the Wenchuan earthquake. The spatial coincidence of these landslides with measured denudation rates is consistent with landslides sustaining denudation fluxes across a wide range of timescales.

Additional second-order features in the exhumation data from the Longmen Shan include two local high rates to the west (Figure 2e), beyond the region of most active landsliding associated with the Wenchuan earthquake. The extent to which these high rates are also explained by earthquake-triggered landsliding is unclear, but some evidence suggests that they might be. The high exhumation rates around 160 km distance along the A-A' transect (Figure 2e) are located along the Wenchuan-Maowen fault (WMF, Figure 2f), another major thrust fault within the Longmen Shan. Rapid exhumation in this region has been attributed to active thrusting of the WMF in the late Cenozoic [Tian et al., 2013 and references therein]. Accompanying seismic activity could have triggered earthquake-triggered landsliding, converting uplifted mass to clastic sediment, enhancing denudation fluxes, and leaving imprints in the exhumation rates seen today. The other zone of locally elevated rates, closer to the plateau (Figure 2e), is less well-defined: moderately high values are recorded by the cosmogenic nuclides and seen in part of the AFT data from Arne et al. (1997) but not in other data (e.g., ZFT). A potential local maximum in denudation rate coincides with a local peak of seismic moment release (Figure 2f, A-A' distance around 200 km) as calculated from short-term historic seismicity (1970-2015) [CSN Catalog, 2015]. Local clustering of seismicity might indicate the potential for landslide-triggering earthquakes in this region. Further low-temperature thermochronology would help to better constrain the exhumation pattern across the Longmen Shan and the linkage between exhumation and co-seismic landsliding.

4.1.2. Seismic control on focused denudation of the Longmen Shan

In addition to seismicity, several other features also vary along the profiles shown in Figures 1 and 2, potentially influencing spatial patterns of denudation [e.g., Burbank et al., 2003; Ouimet et al., 2009]. To distinguish these effects, we have examined the relationships between denudation rates inferred from post-earthquake gauging data (2008-2012) and a group of metrics of topography (slope, relief), hydrology (mean annual runoff, proportion of runoff from high intensity runoff events), fluvial erosion potential (stream power and normalized channel steepness index), seismic shaking (PGA, distance to fault rupture as a metric for seismic energy release), and the density of earthquake-triggered landslides (Figures 3 and 4). Using principle component analysis (PCA), these metrics cluster into two statistically distinct groups that reflect mechanistically distinct processes: (1) a "seismic component", comprising PGA,

landslide volumetric density and distance to fault rupture; and (2) a "non-seismic component," comprising slope angles, relief, steepness index, and the hydrological metrics (for detailed PCA results, see Figure S5, Table S4 and Table S5 and text in Supporting Information).

Across the non-seismic metrics, post-Wenchuan denudation rates correlate positively but moderately ($r^2 = 0.36$, $P < 0.05$, Figure 3a) with the proportion of catchment runoff from high intensity runoff events (> 6 mm day^{-1}), consistent with the findings of Wang et al. [2015a]. Pre-Wenchuan denudation rates also show a moderate, positive correlation with intense runoff events ($r^2 = 0.33$, $P < 0.05$, Figure 3a), but with a shallower slope than post-earthquake rates. The steeper slope of the post-earthquake data indicates that the denudation rate has become more sensitive to hydrological conditions under enhanced sediment supply following the earthquake. We find no correlation between denudation rates and mean annual catchment runoff. There are also no statistically significant correlations between the post-Wenchuan denudation rates and other non-seismic metrics including channel steepness index and stream power (Figure 3b, c, d, e and f), perhaps because landscape steepness exceeds the threshold where these relationships are easily observed [e.g., Ouimet et al., 2009].

For seismic metrics (Figure 4), we find statistically significant correlations between post-Wenchuan denudation rates and catchment-scale mean PGA ($r^2 = 0.61$, $p < 0.002$, Figure 4a), catchment-scale maximum PGA ($r^2 = 0.64$, $p < 0.001$, Figure 4b), distance to the fault rupture ($r^2 = 0.67$, $p < 0.001$, Figure 4c), and the volumetric density of earthquake-triggered landslides ($r^2 = 0.66$, $p < 0.01$, Figure 4d). Although USGS ShakeMap PGA data do not include local site effects and topographic amplification that may affect landslide occurrence, we expect these to have limited influence on the first-order spatial patterns that indicate a seismic control on denudation rates.

Since the principal component analysis separates these seismic parameters from the non-seismic metrics, we do not expect cross-correlation between these two groups (e.g., between PGA and catchment slope or runoff, Figure S6) to bias our interpretations. Seismic intensity and denudation rates co-vary both across the plateau margin (i.e., along A-A'), and also along strike of the range. While the former gradient coincides to some extent with changes in relief, slope, and runoff, the latter does not, emphasizing the seismic role in denudation.

The spatial coverage of the longer-term denudation rate data is not sufficient to conduct a similar analysis, but the correlations described here show that seismicity in the Longmen Shan is not inextricably coupled to other parameters that influence denudation rates. The correlation between sediment flux-derived denudation rates and seismic parameters suggests that the coincidence of high denudation rates and intensive landsliding along the frontal Longmen Shan reflects a seismic driver of denudation, rather than a coincidental relationship with an underlying control by topographic or other non-seismic parameters. We expect that the seismic control on

post-earthquake denudation rates as observed via sediment fluxes would recur for repeated earthquakes, providing a mechanism for seismicity to influence the longer-term pattern and rate of denudation.

We next consider the theoretical magnitude of denudation rate sustained by earthquake-triggered landsliding over multiple earthquake cycles (Section 4.2). We then compare these estimated rates of seismic erosion with the rates measured across timescales (Section 4.3).

4.2. Quantifying seismic erosion rates

4.2.1. Predictions of landslide volumes

Calculating a seismic erosion rate following Eq. 1 depends on predicting landslide volumes associated with earthquakes of varying magnitude. In Figure 5, we show results from the three predictive landslide volume models considered here: the global empirical regression of Malamud et al. (2004), the global seismologically-based model of Marc et al. (2016b), and the Longmen Shan-specific model. We compare these predictions to the volumes of landslides triggered by the Wenchuan and Lushan earthquakes, as determined from landslide mapping [Li et al., 2014; Xu et al., 2015]. The global empirical regression systematically underestimates the volumes of the Wenchuan and the Lushan landslides (Figure 5a). The Longmen Shan model accurately predicts both the Wenchuan and the Lushan landslide volumes (Figure 5b). The global seismologically-based model of Marc et al. (2016b) fits the observations if adjustable parameters in the model are tuned (Figures 5c,d).

In more detail, the results of the global model of Marc et al. (2016b) are sensitive to the adopted parameters, including landscape steepness, mean asperity depth and hillslope material sensitivity. Whereas slope and asperity depth can be determined from DEM and seismological data, respectively, we lack independent constraints on the term describing material sensitivity, which is related to rock strength and pore pressure. Using a global average material sensitivity (as reported by Marc et al., 2016b) and local parameters describing seismology and topography, this model under-predicts the landslide volumes for both the Wenchuan and the Lushan earthquakes (Figure 5c). The model fits the Wenchuan and the Lushan observations for increases in the material sensitivity term of 6 times and 4.3 times, respectively. Model results for a $5\times$ increase in material sensitivity (determined by the minimization of the sum of the squared residuals) closely approximate both volumes (Figure 5d).

Differences in curvature between the two seismologically-based V_L-M_w relations (Figure 5b vs. 5d) derive from assumptions about ground motion attenuation and the landslide volume-ground motion scaling relation. Marc et al. (2016b) assumed (i) a linear relationship between landslide volume and ground motion, in contrast to the non-linear relationship from Wenchuan-specific observations (Figure S3), and (ii) a significant “saturation” effect of ground motion at high earthquake magnitude,

thought to describe attenuation of high-frequency (e.g., 1 Hz) spectral accelerations [e.g., Boore and Atkinson, 2008]. Thus the Marc et al. (2016b) model predicts that ground motion and landslide volumes should increase only slightly with magnitude for large (M_w > ~6.5) earthquakes. Since the magnitude dependence is small, a ~5 km shallower asperity depth is needed in this model to explain the much greater landslide volume from the Wenchuan earthquake (M_w=7.9; V_L=2.7-4.4 km^3) vs. the Lushan event (M_w=6.6; V_L = 0.042 km^3 from Xu et al., 2015, although Marc et al., 2016b quoted a lower volume for this event), assuming similar material sensitivity.

4.2.2. Seismic erosion rates

The Longmen Shan earthquake frequency-magnitude distribution depends on the recurrence interval for Wenchuan-like events, T (Section 3.6.3, Figure 6a); across the range of plausible estimates for T (~500-4000 years), we find a lower seismic erosion rate with longer T (Figure 5b). For a given T, the corresponding seismic erosion rate also differs depending on the landslide volume model (Figure S7). Using the Longmen Shan seismologically-based landslide volume model (Figure 5b), we calculate an erosion rate of 0.44-0.96 mm yr^{-1} (with a central estimate of 0.51-0.81 mm yr^{-1}), which reduces to 0.34-0.81 mm yr^{-1} (with a central estimate of 0.40-0.69 mm yr^{-1}) taking into account focal depth (Figure 6b). The rates calculated using the global empirical regression [Keefer, 1994] and the global seismologically-based model [Marc et al., 2016b] are lower than the result using our Longmen Shan-specific model. This outcome is not surprising, since the two former models underestimate the observed landslide volumes for Wenchuan and Lushan, a discrepancy that we attribute to uncertainties in applying globally-calibrated parameters to a specific region (see Section 4.3.1, above). On the other hand, using the global seismologically-based model with the ~5× increase in material sensitivity that captures the observed Longman Shan volumes (Figure 5d) yields a seismic erosion rate of 0.37-1.68 mm yr^{-1}, with a central estimate of 0.73-0.99 mm yr^{-1}, close to that calculated from the Longmen Shan-specific model although slightly higher because of the strong non-linearity of the global model. These comparisons emphasize the sensitivity of landslide erosion calculations to model assumptions, and particularly the importance of using locally calibrated parameters since global average values may not accurately reflect a specific region (as suggested by Keefer, 1994).

4.3. Comparing magnitudes of denudation rates across different timescales

4.3.1. Average denudation rate of the frontal Longmen Shan

The catchment area-weighted means (±1 standard deviation) of pre-Wenchuan and post-Wenchuan denudation rates inferred from hydrological gauging are 0.24±0.04 mm yr^{-1} and 1.09±0.13 mm yr^{-1} respectively. The equivalent average kyr-timescale cosmogenic nuclide-derived denudation rate is 0.55±0.05 mm yr^{-1}. For denudation over Myr timescales, we interpolate the exhumation rates in the intensive erosion zone and run 1,000,000 Monte Carlo random simulations to account for the uncertainties from individual exhumation rate estimates. The resulting Myr denudation rate is 0.61+0.14/-0.08 mm yr^{-1} (uncertainties indicate the 16th and 84th

percentiles of the Monte Carlo results). The inferred seismic erosion rates over multiple earthquake cycles range from 0.34 to 0.81 mm yr^{-1} across the range of plausible T values (500-4000 years), using the Longmen Shan-specific seismologically-based V_L-M_w relation.

4.3.2. Pre- and Post-Wenchuan earthquake sediment fluxes versus long-term denudation rate

The 2006-2007 pre-Wenchuan denudation rate calculated from sediment fluxes is lower than the long-term denudation rate. The rate reported from the 1960s to 1980s gauging data is higher than that calculated from the 2006-2007 data, but still slightly lower than the long-term rate. In contrast, the post-Wenchuan sediment flux-derived denudation rate is the highest amongst all observed denudation rates (Figure 7). The long-term average denudation rates (i.e., from cosmogenics and thermochronology) thus fall between the immediate pre- and post-earthquake values derived from sediment fluxes. In general terms, this pattern is consistent with a conceptual model for erosional dynamics over one complete earthquake cycle in which the pre-earthquake rates reflect below-average values and the post-earthquake rates reflect an immediate post-seismic denudational pulse [Ouimet, 2010]. However, given the large variability in pre-earthquake rates (comparing 2006-2007 data vs. 1960s-1980s), it is difficult to use these data to evaluate quantitatively the extent to which the post-earthquake pulse contributes to the long-term budget; considering the 2006-2007 data alone, the post-earthquake pulse would need to play a major role to make the long-term value, but considering the data from the 1960s-1980s, this role would need to be relatively small over the long term.

4.3.3. Seismic erosion rate vs. long-term denudation rate

Our best estimate of the seismic erosion rate (0.34-0.81 mm yr^{-1}, using the Longmen Shan-specific landslide volume model) is comparable to the measured long-term denudation rates of the frontal Longmen Shan (kyr denudation rate: 0.55±0.05 mm yr^{-1}; Myr exhumation rate: 0.61+0.14/-0.08 mm yr^{-1}) (Figure 7). Using the global seismologically-based model for landslide volumes yields a slightly higher calculated denudation rate via earthquake-induced landslides (0.37-1.68 mm yr^{-1}, with central estimate of 0.73-0.99 mm yr^{-1}; Figure S7). Denudation rates determined either from gauging data and long-term chronometers include mass loss via dissolved load in addition to via physical erosion. If dissolved load is mainly derived from weathering of landslide material [e.g., Emberson et al., 2016], the calculated seismic erosion rate should be directly comparable to the denudation rate. Significant non-landslide solute sources, such as from ground water release [e.g., Jin et al., 2016], would increase the denudation rate compared to the calculated seismic erosion rates, although such effects should be small since dissolved load represents a relatively low proportion of the total denudation flux (~20%, Section 3.4). Either way, additional dissolved load contributions would not explain a lower measured denudation rate compared to the calculated seismic erosion rate.

We recognize that not all landslide material is necessarily evacuated from a mountain belt by rivers within one earthquake cycle. Landslide erosion rates could be higher than actual measured long-term denudation rates if new seismically triggered landslides re-mobilize debris associated with prior earthquakes. Given the relatively rapid rates of sediment evacuation observed in the Longmen Shan region compared to the long earthquake recurrence times [Liu et al., 2013] and the lack of extensive storage of intra-montane landslide debris in this setting [Parker et al., 2011], we view near-complete evacuation as a reasonable first-order assumption for comparing rates. If this is the case, the seismic erosion rates calculated from the Longmen Shan-specific landslide volume model are consistent with the measured long-term denudation rates.

Whether the seismic erosion rate is similar in magnitude or slightly higher than the measured long-term rate (Figure 7), our results demonstrate that, at least in this region, earthquake-triggered landslides are capable of sustaining denudation rates that are comparable to long-term averages at the mountain belt scale and over timescales of multiple seismic cycles. A corollary is that the observed erosional fluxes are likely to be dominated by material derived from earthquake-triggered landslides, with implications not only for sediment dynamics and landscape evolution, but also for biogeochemical cycles [e.g., Jin et al., 2016; Emberson et al., 2016].

Over longer timescales, climate fluctuations may influence the capacity of the sediment routing systems for removing landslide debris and maintaining river incision and hillslope weathering rates required to sustain landslides. Indeed, we find that high intensity runoff events help to explain the observed short-term denudation rates in the Longmen Shan (Fig. 3a), pointing to the importance of climate variability as an erosional agent. Thus we expect that climate – which may have changed in response to topographic evolution [e.g., Molnar et al., 2010] – interacts with seismic events to influence the pace of surface processes in the Longmen Shan, even though a primary control may be related to the seismotectonic processes that trigger landslides and thus convert rocks to erodible sediment. Our results suggest that earthquake-triggered landslides can focus denudation in mountains where rivers have the capacity to transport and export the excess sediment supplied from hillslopes (e.g. Fig. 3a). In these settings the denudation can be considered as tectonically limited [Montgomery and Brandon, 2002], yet fully understanding topographic evolution will require better understanding how landslide frequency and magnitude, and the associated fluvial export of sediment, respond to long-term climatic fluctuations.

5. Conclusions and Implications

By considering the effects of multiple earthquakes, we calculate that co-seismic landslides can sustain denudation rates that are similar to the rates recorded by chronometers over timescales of thousands to millions of years (Figure 7). In addition to similar magnitudes, we find a first-order spatial coincidence of long-term denudation and Wenchuan-triggered landslides (Section 4.1, Figure 2), and a

correlation between the sediment-derived denudation rates and co-seismic landsliding (Figure 4d). Over the long term, the location of earthquake-triggered landslides should reflect earthquake sources and ground motion attenuation, with landslide density decreasing away from seismogenic faults [Meunier et al., 2007], as we also observe for the Wenchuan case.

Our observations suggest that the long-term location and rate of denudation in the Longmen Shan is consistent with the focusing of seismic energy release along range-bounding faults, with the resulting landslides serving as a primary mechanism sustaining denudation fluxes. Landslides can only continue to operate as effective denudation mechanisms if hillslopes are sufficiently steep. It is likely that the combination of uplift, river incision, and fluvial evacuation of sediment [e.g., Burbank et al., 1996; Bennett et al., 2016] is capable of continually re-steepening and re-weakening failed landscapes between earthquake cycles. Earthquakes should increase the efficiency of landslide generation for a given steepness and hillslope strength, such that the location of most intense erosion at the orogenic scale may be determined by seismic energy release. These effects could be enhanced by rock weakening resulting from greater deformation and orographic rainfall close to mountain fronts [Gallen et al., 2015; Vanmaercke et al., 2017]. We thus suggest that focused denudation along a high-relief plateau margin may be regulated at least in part by the location and activity of seismogenic faulting, and specifically by the resulting earthquake-triggered landslides.

Acknowledgements

This research was supported by the U.S. National Science Foundation (NSF-EAR/GLD grant 1053504 to A.J.W.) and the Chinese Academy of Sciences (YIS fellowship grant 2011Y2ZA04 to A.J.W.). G.L. was supported by the USC Dornsife College Merit Fellowship and a GSA graduate student research grant. This work benefited from conversations with Sean Gallen, Niels Hovius, Odin Marc, Haoran Meng, Joel Scheingross, James Dolan and Seulgi Moon. We thank constructive comments from an anonymous reviewer that greatly helped to improve an earlier version of the manuscript and An Yin for editorial handling.

Figure 1.

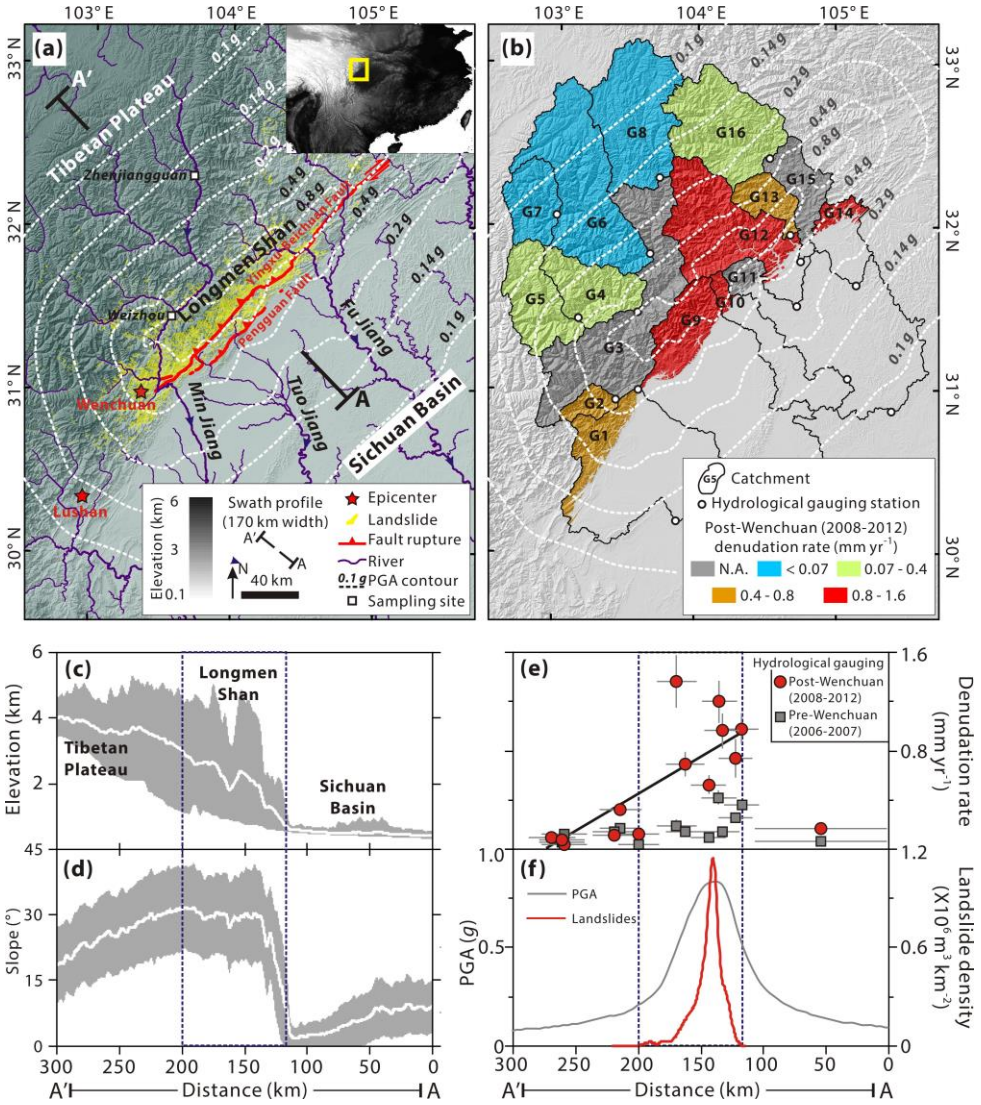

Figure 1. Maps of topography of the study area, locations of the M_w7.9 2008 Wenchuan and the M_w6.6 2013 Lushan earthquakes, the Wenchuan peak ground accelerations (PGA) (gridded data from the USGS hazards program, http://earthquake.usgs.gov/earthquakes), Wenchuan-triggered landslides and post-Wenchuan gauging-derived denudation rates, and swath profiles of topography, denudation rates, PGA, and landslides. (a) Map of the M_w7.9 2008 Wenchuan earthquake and the M_w6.6 Lushan earthquake epicenters (red stars), mapped Wenchuan earthquake-triggered landslides (yellow polygons) over shaded relief map, Wenchuan PGA contours (dashed lines), the trend of the 170 km-wide swath profile (A-A'), sampling sites of river water samples (Jin et al., 2016) (squares), Wenchuan earthquake surface rupture (red lines), and the regional context of the study area (inset panel); (b) map of post-seismic sediment flux-derived denudation rates upstream of hydrological gauging stations (circles); denudation rates are normalized to areas with

elevation > 800 m to account for limited contribution from flat frontal plains; (c) swath profile of the topography projected along A-A' showing the mean (white line) and maximum and minimum elevations (grey area); blue dashed lines delimit the zone with intensive denudation between profile distances of 120 km and 200 km); (d) swath profile of slopes ( ) projected along A-A' with mean slope (white line) ±1 standard deviation on the mean slope (grey area); (e) swath profile of pre-Wenchuan earthquake (2006-2007, red circles) and post-Wenchuan earthquake (2008-2012, grey squares) denudation rates (y-axis error bars = ±1 s.d. uncertainties in denudation rates, x-axis error bars = square root of catchment area), the decreasing trend of post-seismic denudation rates along the swath is shown by least-squares fitting of denudation vs. distance along A-A' (solid black line); for denudation in the frontal Sichuan basin, we divide the estimated denudation fluxes by the total catchment area including areas with elevation < 800 m, and this provides an upper limit; (f) swath profiles sampled at 5 km-intervals along A-A' of PGA (grey) and the volumetric density for all landslides (red, m^3 km^{-2}, landslide volume over the specified area).

Figure 2.

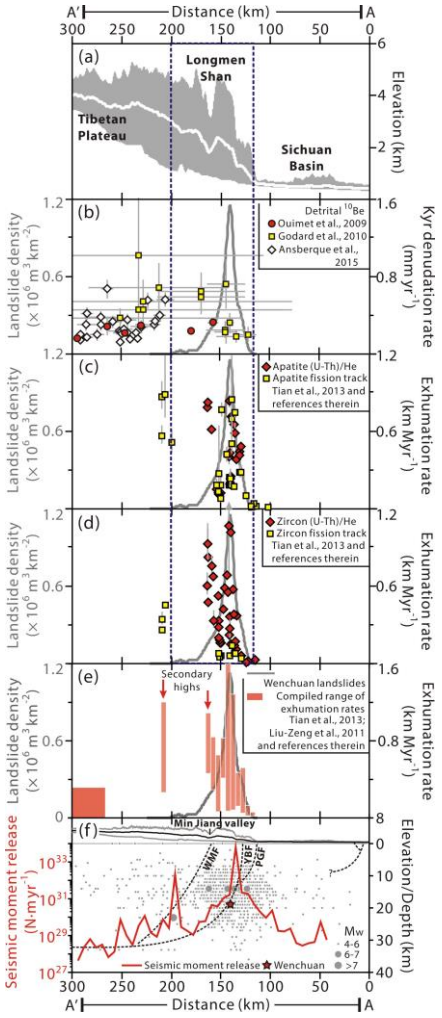

Figure 2. Swath profiles of topography, millennial denudation rates, geological exhumation rates and seismicity across the Longmen Shan range. (a) Swath profile of topography along the Longmen Shan range (A-A'); white line – mean elevations; grey area – minimum-maximum elevation envelop; blue dashed lines bound the intensive denudation zone as defined in Figure 1; (b) swath profile of ^{10}Be-derived millennial denudation rates; error bars on the y-axis indicate ±1 s.d. uncertainties, and on the x-axis the square roots of the catchment area; (c) swath profile of apatite fission track (AFT) and apatite (U-Th)/He (AHe)-determined exhumation rates; error bars are ±1 s.d. uncertainties; (d) swath profile of zircon (U-Th)/He (ZHe) and zircon fission track (ZFT)-determined exhumation rates with ±1 s.d. uncertainties (error bars); (e) swath profile of compiled exhumation rates (red bars: range of exhumation rates including uncertainties; for data with distance < 250 km, data points are binned in 5 km-wide increments); the grey curves on (b), (c), (d) and (e) show the Wenchuan landslide distribution, as in Figure 1f; (f) swath profiles of topography (black solid curve: mean elevations; grey solid curves: minimum and maximum elevations), historic seismicity (1970-2015, grey circles sized by the estimated magnitude; star: Wenchuan

earthquake) [CSN Catalog, 2015] and seismic moment release (red curve, data binned in 5 km-wide increments), and a simplified sketch of the Longmen Shan fault system (WMF: Wenchuan-Maowen fault; YBF: Yingxiu-Beichuan fault; PGF: Pengxian-Guanxian fault) [Liu-Zeng et al., 2011; Ansberque et al., 2015 and references therein].

Figure 3.

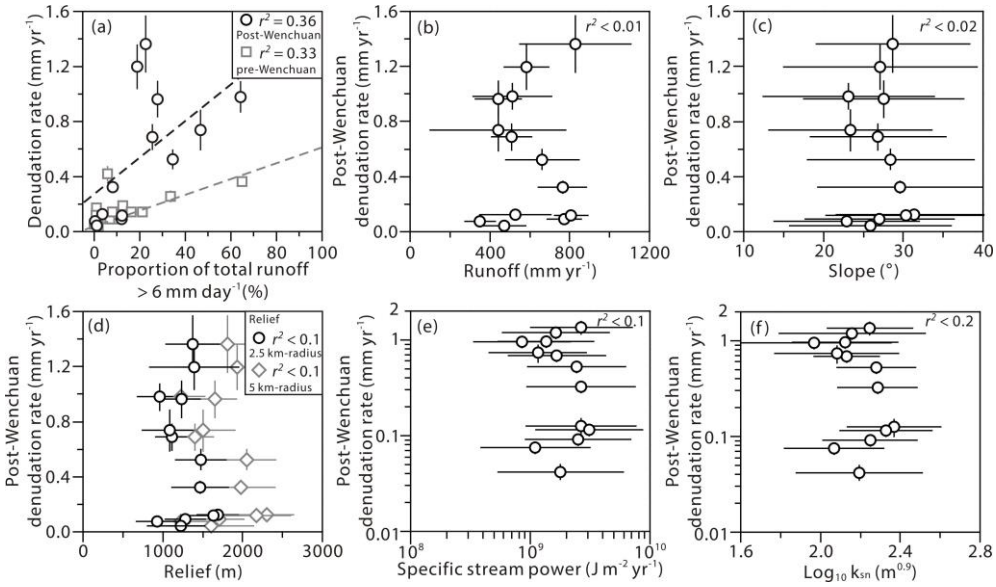

Figure 3. Sediment flux-derived denudation rates for the catchments draining the Longmen Shan plotted versus hydrological and topographic metrics. (a), Post-Wenchuan (circles) and pre-Wenchuan (squares) denudation rate as a function of the proportion of total runoff from days with runoff > 6 mm day^{-1}; post-Wenchuan denudation rate plotted versus annual runoff (b), slope (c), and relief (d); relief is calculated as the ranges of elevations over 2.5 km-radius (circles) and 5 km-radius (diamonds) circular windows. (e), Post-Wenchuan denudation rate against specific stream power calculated using the approach in Burbank et al., (2003) and Ansberque et al. (2015). (f), Post-Wenchuan denudation rate vs. normalized channel steepness index calculated using Stream Profiler (http://www.geomorphtools.org) and normalized to θ_{ref} = 0.45. All error bars represent ±1 s.d. uncertainties.

Figure 4.

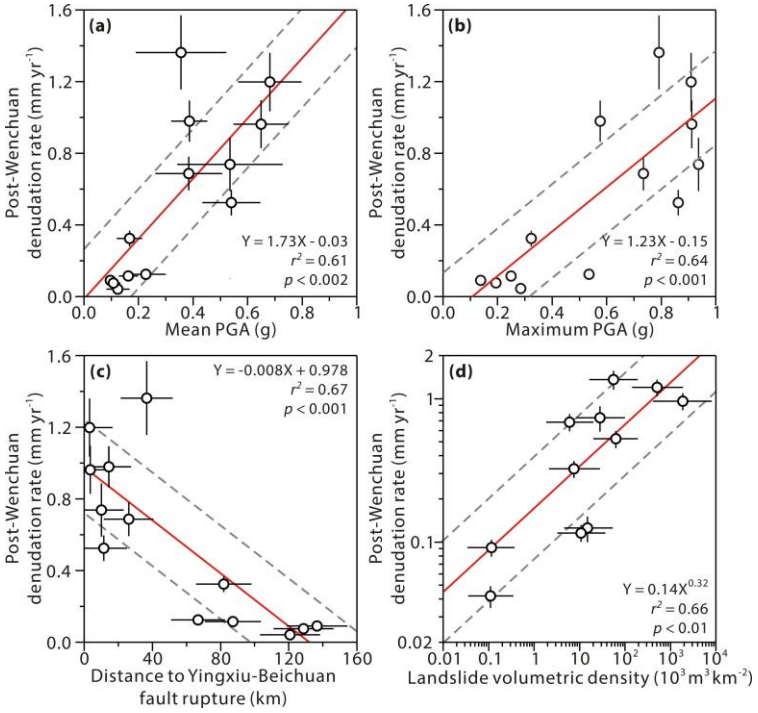

Figure 4. Relationships between sediment flux-derived denudation rates and seismic parameters. Post-Wenchuan denudation rate as a function of: (a) catchment mean PGA; (b) catchment maximum PGA; (c) mean distance of each catchment to the Yingxiu-Beichuan fault rupture; and (d) landslide volumetric density. Red solid lines show best fits from linear least-squares regression (performed in the logarithmic space for d); grey dashed lines show ±1 s.d. uncertainties of the fits; error bars for denudation and PGA indicate ±1 s.d. uncertainties; error bars for distance to the fault rupture are the square roots of catchment area; landslide volumetric densities are reported as the median values and the 16th and 84th percentiles of the distribution (i.e., ranges of ±1 s.d. in a standard normal distribution) from the results from 1000 Monte Carlo random sampling simulations.

Figure 5.

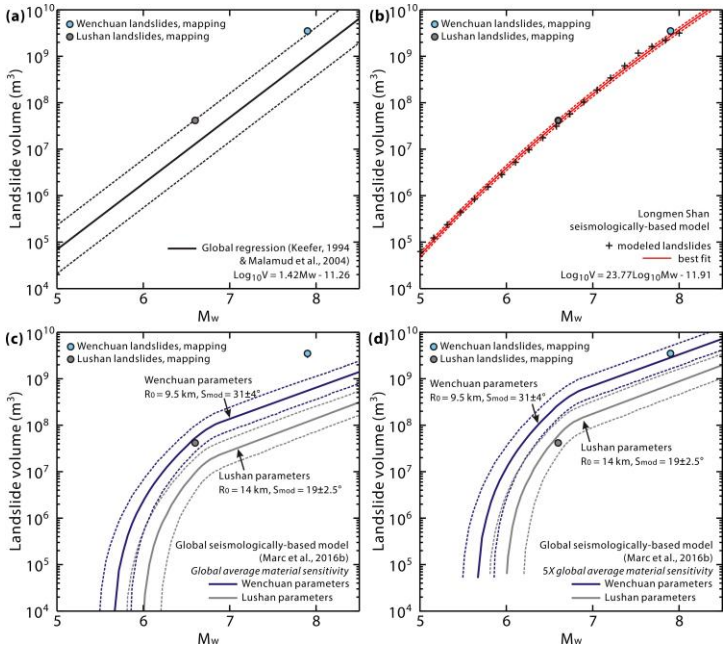

Figure 5. Earthquake-triggered landslide volume models. (a) Global empirical regression between earthquake magnitude and associated landslide volume [Keefer, 1994; Malamud et al., 2004]; solid line represents the logarithmic least squares linear fit; dashed lines show ±1 s.d. uncertainties (residual errors) of the fit; the blue and the grey circles are Wenchuan and the Lushan data, respectively; (b) Longmen Shan-specific, seismologically-based landslide volume model; the crosses represent the modeled landslide volumes for 20 earthquakes with magnitude from 5 to 8; the solid curve represents the best fit of the modeled landslide volumes as a function of earthquake magnitude (details in the Supporting Information); the dashed curves show ±1 s.d. uncertainties (residual errors) of the fit; (c) a global seismologically-based landslide volume model [Marc et al., 2016b]; the blue and grey curves refer to the modeled landslide volumes using the Wenchuan parameters (mean asperity depth = 9.5 km, modal slope = 31 ±4 °, uncertainty: range at 98% of modal slope frequency defined in Marc et al., 2016b) and the Lushan parameters (mean asperity depth = 14 km, modal slope = 19 ±2.5 °, uncertainty: range at 98% of modal slope frequency defined in Marc et al., 2016b), respectively, both using global average material sensitivity; dashed curves show 68% confidence interval from Monte Carlo simulations accounting for uncertainties of the relevant parameters (Marc et al., 2016b; details in Supporting Information); (d) the modeled results from the model of Marc et al. 2016b with 5 × material sensitivity.

Figure 6.

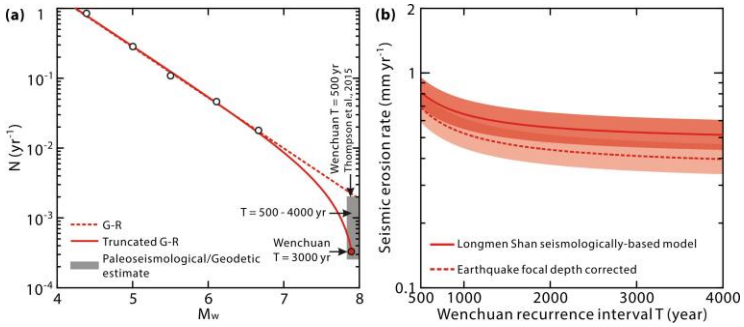

Figure 6. Earthquake magnitude-frequency distribution of the Longmen Shan region, and the calculated seismic erosion rate. (a) Longmen Shan earthquake magnitude-frequency relation described by a truncated Gutenberg-Richter relation [Utsu, 1999] using historic seismicity data (white circles) [Wang et al., 2015b] and the recurrence interval (T) for Wenchuan-like events from paleoseismological/geodetic studies (grey-shaded zone); red dot and solid curve – truncated G-R relation for T = 3000 years [Shen et al., 2009]; dashed line – linear G-R relation, which fits T ~ 500 years [Thompson et al., 2015]; (b) calculated seismic erosion rate with the Longmen Shan seismologically-based landslide volume model as a function of the estimated recurrence interval for Wenchuan-alike events, T; shaded area shows ±1 s.d; the solid curve shows results assuming landslides are triggered by all simulated earthquakes; the dashed curve includes a threshold focal depth for earthquake triggering.

878

879 Figure 7.

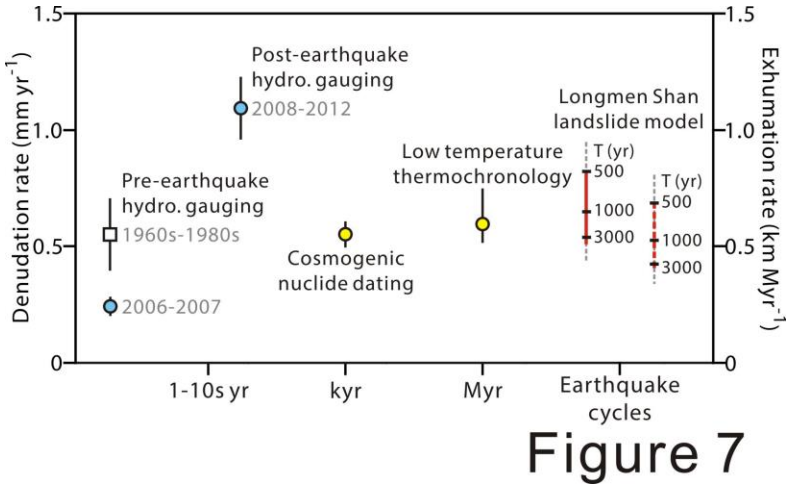

880

881 Figure 7. Denudation rates of the frontal Longmen Shan across different timescales.
882 The blue circles show pre-Wenchuan and post-Wenchuan earthquake denudation rates
883 determined from hydrological gauging; the square shows pre-Wenchuan earthquake
884 (1960s-1980s) denudation rates reported in Liu-Zeng et al. (2011); yellow circles
885 show long-term denudation rates determined from ^{10}Be measurements and low
886 temperature thermochronology analysis (AFT and AHe). For catchment-scale
887 denudation (river gauging and ^{10}Be studies), the denudation rates are the catchment
888 area-weighted means, and the error bars represent catchment area-weighted 1 s.d.
889 uncertainty. For the low temperature thermochronology-based denudation estimate,
890 the denudation rate is reported as the average after interpolating the exhumation data
891 compiled in Tian et al. (2013), with uncertainties propagated from the reported
892 uncertainties in individual exhumation rate estimate [Tian et al., 2013]. Red bars with
893 black ticks show seismic erosion rates across the range of estimated Wenchuan
894 recurrence intervals (T=500-4000 years), with a solid red bar for all earthquakes, a
895 dashed red bar considering focal depth threshold (see Fig. 6), and black ticks for noted
896 T values; dashed grey line = 1 s.d. uncertainties.

897

Table 1. Notation for symbols

Symbol	Notation	Unit
A	Area of landslide occurrence over earthquake cycles	km^2
c_1 c_2 c_3 c_4	Parameters of ground motion attenuation equation, Longmen Shan	
D	Distance to fault rupture	km
$\dot{e}$	Seismic erosion rate	mm yr^{-1}
k_{sn}	Normalized channel steepness index	$m^{0.9}$
M_w	Earthquake moment magnitude	-
$N(M_w)$	Number of earthquakes in the magnitude bin [M_w, M_w + 0.1]	
R_0	Mean asperity depth	km
S_{mod}	Modal slope	°
t	Time period of multiple earthquake cycles	yr
T	Recurrence interval for Wenchuan-like earthquakes	yr
V_L	Landslide volume	m^3
θ_{ref}	Reference concavity index	–
ω	Specific stream power	J m^{-2} yr^{-1}

References

Ansberque, C., V. Godard, O. Bellier, J. De Sigoyer, J. Liu-Zeng, X. Xu, Z. Ren, Y. Li, and A. S. T. E. R. Team (2015), Denudation pattern across the Longriba fault system and implications for the geomorphological evolution of the eastern Tibetan margin, Geomorphology, 246, 542-557, doi: 10.1016/j.geomorph.2015.07.017.

Arne, D., B. Worley, C. Wilson, S. F. Chen, D. Foster, Z. L. Luo, S. G. Liu, and P. Dirks (1997), Differential exhumation in response to episodic thrusting along the eastern margin of the Tibetan Plateau, Tectonophysics, 280(3–4), 239-256, doi: 10.1016/S0040-1951(97)00040-1.

Bennett, G. L., S. R. Miller, J. J. Roering, and D. A. Schmidt (2016), Landslides, threshold slopes, and the survival of relict terrain in the wake of the Mendocino Triple Junction, Geology, doi: 10.1130/g37530.1.

Beaumont, C., R. A. Jamieson, M. H. Nguyen, and B. Lee (2001), Himalayan tectonics explained by extrusion of a low-viscosity crustal channel coupled to focused surface denudation, Nature, 414(6865), 738-742, doi: 10.1038/414738a.

Burchfiel, B. C., L. H. R., R.D. van der Hilst, B.H. Hager, Z. Chen, R.W. King, C. Li, J. Lü, H. Yao, and E. Kirby (2008), A geological and geophysical context for the Wenchuan earthquake of 12 May 2008, Sichuan, People's Republic of China, GSA Today, 18(7), 5, doi: 10.1130/GSATG18A.1.

Burbank, D. W., J. Leland, E. Fielding, R. S. Anderson, N. Brozovic, M. R. Reid, and C. Duncan (1996), Bedrock incision, rock uplift and threshold hillslopes in the northwestern Himalayas, Nature, 379(6565), 505-510, doi:10.1038/379505a0.

Burbank, D. W., A. E. Blythe, J. Putkonen, B. Pratt-Sitaula, E. Gabet, M. Oskin, A. Barros, and T. P. Ojha (2003), Decoupling of erosion and precipitation in the Himalayas, Nature, 426(6967), 652-655, doi:10.1038/nature02187.

Clark, M. K., and L. H. Royden (2000), Topographic ooze: Building the eastern margin of Tibet by lower crustal flow, Geology, 28(8), 703-706, doi: 10.1130/0091-7613(2000)28<703:tobtem>2.0.co;2.

CSN Catalog (2015), data collected by the China Seismograph Network stations, Copyrighted & produced by China Earthquake Networks Center (CENC) (http://www.csndmc.ac.cn/wdc4seis@bj/earthquakes/csn_catalog_p001.jsp)

Cui, J.W., J.G. Zhang, D. Gao, J.X. Duan and T. Wang (2012), The ground motion attenuation relation for the Mountainous area in Sichuan and Yunnan, 15th World Conference on Earthquake Engineering 2012, 1, 668-677.

Densmore, A. L., M. A. Ellis, Y. Li, R. J. Zhou, G. S. Hancock, and N. Richardson (2007), Active tectonics of the Beichuan and Pengguan faults at the eastern margin of the Tibetan Plateau, Tectonics, 26(4), doi: 10.1029/2006tc001987.

Emberson, R., N. Hovius, A. Galy, and O. Marc (2016), Chemical weathering in active mountain belts controlled by stochastic bedrock landsliding, Nature Geoscience, 9(1), 42-45, doi: 10.1038/ngeo2600.

Gallen, S. F., M. K. Clark, and J. W. Godt (2015), Coseismic landslides reveal near-surface rock strength in a high-relief, tectonically active setting, Geology, 43(1), 11-14, doi: 10.1130/g36080.1.

Godard, V., J. Lave, J. Carcaillet, R. Cattin, D. Bourles, and J. Zhu (2010), Spatial distribution of denudation in Eastern Tibet and regressive erosion of plateau margins, Tectonophysics, 491(1-4), 253-274, doi: 10.1016/j.tecto.2009.10.026.

949 Godard, V., R. Pik, J. Lave, R. Cattin, B. Tibari, J. de Sigoyer, M. Pubellier, and J. Zhu (2009), Late
950 Cenozoic evolution of the central Longmen Shan, eastern Tibet: Insight from (U-Th)/He
951 thermochronometry, Tectonics, 28, TC5009, doi: 10.1029/2008tc002407.
952 Hovius, N., P. Meunier, L. Ching-Weei, C. Hongey, C. Yue-Gau, S. Dadson, H. Ming-Jame, and M.
953 Lines (2011), Prolonged seismically induced erosion and the mass balance of a large earthquake,
954 Earth and Planetary Science Letters, 304(3-4), 347-355, doi: 10.1016/j.epsl.2011.02.005.
955 Hubbard, J., and J. H. Shaw (2009), Uplift of the Longmen Shan and Tibetan plateau, and the 2008
956 Wenchuan (M=7.9) earthquake, Nature, 458(7235), 194-197, doi: Doi 10.1038/Nature07837.
957 Jarvis, A., H.I. Reuter, A. Nelson, E. Guevara, 2008, Hole-filled SRTM for the globe Version 4,
958 available from the CGIAR-CSI SRTM 90m Database (http://srtm.csi.cgiar.org).
959 Jin, Z., A. J. West, F. Zhang, Z. An, R. G. Hilton, J. Yu, J. Wang, G. Li, L. Deng, and X. Wang (2016),
960 Seismically enhanced solute fluxes in the Yangtze River headwaters following the A.D. 2008
961 Wenchuan earthquake, Geology, 44(1), 47-50, doi: 10.1130/g37246.1.
962 Keefer, D. K. (1994), The Importance of Earthquake-Induced Landslides to Long-Term Slope Erosion
963 and Slope-Failure Hazards in Seismically Active Regions, Geomorphology, 10(1-4), 265-284, doi:
964 10.1016/0169-555x(94)90021-3.
965 Kirby, E., P. W. Reiners, M. A. Krol, K. X. Whipple, K. V. Hodges, K. A. Farley, W. Tang, and Z. Chen
966 (2002), Late Cenozoic evolution of the eastern margin of the Tibetan Plateau: Inferences from
967 40Ar/39Ar and (U-Th)/He thermochronology, Tectonics, 21(1), doi: 10.1029/2000tc001246.
968 Larsen, I. J., D. R. Montgomery, and O. Korup (2010), Landslide erosion controlled by hillslope
969 material, Nature Geoscience, 3(4), 247-251, doi: 10.1038/ngeo776.
970 Larsen, I. J., D. R. Montgomery, and H. M. Greenberg (2014), The contribution of mountains to global
971 denudation, Geology, doi: 10.1130/g35136.1.
972 Lavé, J., and D. Burbank (2004), Denudation processes and rates in the Transverse Ranges, southern
973 California: Erosional response of a transitional landscape to external and anthropogenic forcing,
974 Journal of Geophysical Research: Earth Surface, 109(F1), 1-31, doi: 10.1029/2003jf000023.
975 Li, G., A. J. West, A. L. Densmore, Z. Jin, R. N. Parker, and R. G. Hilton (2014), Seismic mountain
976 building: Landslides associated with the 2008 Wenchuan earthquake in the context of a generalized
977 model for earthquake volume balance, Geochemistry, Geophysics, Geosystems, 15(4), 833-844, doi:
978 10.1002/2013gc005067.
979 Li, G., A. J. West, A. L. Densmore, D. E. Hammond, Z. Jin, F. Zhang, J. Wang, and R. G. Hilton (2016),
980 Connectivity of earthquake-triggered landslides with the fluvial network: Implications for landslide
981 sediment transport after the 2008 Wenchuan earthquake, Journal of Geophysical Research: Earth
982 Surface, 121(4), 703-724, doi: 10.1002/2015jf003718.
983 Liu, F, B.H. Fu, S.H. Yang (2013) Quantitative estimation of the evacuation time of landslide mass and
984 sediment induced by the 2008 Wenchuan great earthquake along the Minjiang River, Longmen Shan
985 in east Tibet, Chinese Journal of Geophysics, 56(5), 1517–1525. (in Chinese with English abstract)
986 Liu-Zeng, J., L. Wen, M. Oskin, and L. S. Zeng (2011), Focused modern denudation of the Longmen
987 Shan margin, eastern Tibetan Plateau, Geochemistry Geophysics Geosystems, 12, Q1107, doi:
988 10.1029/2011gc003652.
989 Malamud, B. D., D. L. Turcotte, F. Guzzetti, and P. Reichenbach (2004), Landslides, earthquakes, and
990 erosion, Earth and Planetary Science Letters, 229(1–2), 45-59, doi: 10.1016/j.epsl.2004.10.018.
991 Marc, O., N. Hovius, and P. Meunier (2016a), The mass balance of earthquakes and earthquake
992 sequences, Geophysical Research Letters, 43(8), 3708-3716, doi: 10.1002/2016gl068333.

993 Marc, O., N. Hovius, P. Meunier, T. Gorum, and T. Uchida (2016b), A seismologically consistent
994 expression for the total area and volume of earthquake-triggered landsliding, Journal of Geophysical
995 Research: Earth Surface, 121(4), 2015JF003732, doi: 10.1002/2015jf003732.
996 Meunier, P., N. Hovius, and A. J. Haines (2007), Regional patterns of earthquake-triggered landslides
997 and their relation to ground motion, Geophysical Research Letters, 34(20), L20408, doi
998 10.1029/2007gl031337.
999 Molnar, P., and P. England (1990), Late Cenozoic uplift of mountain ranges and global climate change:
1000 chicken or egg?, Nature, 346(6279), 29-34, doi: 10.1038/346029a0.
1001 Molnar, P., W. R. Boos, and D. S. Battisti (2010), Orographic Controls on Climate and Paleoclimate of
1002 Asia: Thermal and Mechanical Roles for the Tibetan Plateau, Annual Review of Earth and Planetary
1003 Sciences, 38(1), 77-102, doi: 10.1146/annurev-earth-040809-152456.
1004 Montgomery, D. R., and M. T. Brandon (2002), Topographic controls on erosion rates in tectonically
1005 active mountain ranges, Earth and Planetary Science Letters, 201(3–4), 481-489, doi:
1006 10.1016/S0012-821X(02)00725-2.
1007 Ouimet, W. B. (2010), Landslides associated with the May 12, 2008 Wenchuan earthquake:
1008 Implications for the erosion and tectonic evolution of the Longmen Shan, Tectonophysics, 491(1-4),
1009 244-252, doi: 10.1016/j.tecto.2009.09.012.
1010 Ouimet, W. B., K. X. Whipple, and D. E. Granger (2009), Beyond threshold hillslopes: Channel
1011 adjustment to base-level fall in tectonically active mountain ranges, Geology, 37(7), 579-582, doi:
1012 10.1130/G30013a.1.
1013 Parker, R. N., A. L. Densmore, N. J. Rosser, M. de Michele, Y. Li, R. Q. Huang, S. Whadcoat, and D. N.
1014 Petley (2011), Mass wasting triggered by the 2008 Wenchuan earthquake is greater than orogenic
1015 growth, Nature Geoscience, 4(7), 449-452, doi: 10.1038/Ngeo1154.
1016 Raymo, M. E., W. F. Ruddiman, and P. N. Froelich (1988), Influence of late Cenozoic mountain
1017 building on ocean geochemical cycles, Geology, 16(7), 649-653, doi:
1018 10.1130/0091-7613(1988)016<0649:iolcmb>2.3.co;2.
1019 Reiners, P. W., and M. T. Brandon (2006), Using thermochronology to understand orogenic erosion,
1020 Annual Reviews of Earth and Planetary Scinces, 34, 419–466, doi:
1021 10.1146/annurev.earth.34.031405.125202.
1022 Richardson, N. J., A. L. Densmore, D. Seward, A. Fowler, M. Wipf, M. A. Ellis, L. Yong, and Y. Zhang
1023 (2008), Extraordinary denudation in the Sichuan Basin: Insights from low-temperature
1024 thermochronology adjacent to the eastern margin of the Tibetan Plateau, Journal of Geophysical
1025 Research: Solid Earth, 113(B4), doi: 10.1029/2006jb004739.
1026 Roback, K., M. Clark, A. J. West, D. Zekkos, G. Li, S. F. Gallen, D. Champlain, J. Godt (2017), The
1027 size, distribution, and mobility of landslides caused by the 2015 M_w7.8 Gorkha earthquake, Nepal,
1028 accepted, Geomorphology
1029 Shen, Z. K., J. B. Sun, P. Z. Zhang, Y. G. Wan, M. Wang, R. Burgmann, Y. H. Zeng, W. J. Gan, H. Liao,
1030 and Q. L. Wang (2009), Slip maxima at fault junctions and rupturing of barriers during the 2008
1031 Wenchuan earthquake, Nature Geoscience, 2(10), 718-724, doi: 10.1038/ngeo636.
1032 Steer, P., M. Simoes, R. Cattin, and J. B. H. Shyu (2014), Erosion influences the seismicity of active
1033 thrust faults, Nature Communications, 5, doi: 10.1038/ncomms6564.
1034 Thompson, T. B., A. Plesch, J. H. Shaw, and B. J. Meade (2015), Rapid slip-deficit rates at the eastern
1035 margin of the Tibetan Plateau prior to the 2008 Mw 7.9 Wenchuan earthquake, Geophysical
1036 Research Letters, 42(6), 1677-1684, doi: 10.1002/2014gl062833.

1037 Tian, Y., B. P. Kohn, A. J. W. Gleadow, and S. Hu (2013), Constructing the Longmen Shan eastern
1038 Tibetan Plateau margin: Insights from low-temperature thermochronology, Tectonics, 32(3), 576-592,
1039 doi: 10.1002/tect.20043.
1040 Utsu, T. (1999), Representation and Analysis of the Earthquake Size Distribution: A Historical Review
1041 and Some New Approaches, pure and applied geophysics, 155(2), 509-535, doi:
1042 10.1007/s000240050276.
1043 Vanmaercke, M., F. Ardizzone, M. Rossi, and F. Guzzetti (2017), Exploring the effects of seismicity on
1044 landslides and catchment sediment yield: An Italian case study, Geomorphology, 278, 171-183, doi:
1045 10.1016/j.geomorph.2016.11.010.
1046 Wang, E., E. Kirby, K. P. Furlong, M. van Soest, G. Xu, X. Shi, P. J. J. Kamp, and K. V. Hodges (2012),
1047 Two-phase growth of high topography in eastern Tibet during the Cenozoic, Nature Geoscience, 5(9),
1048 640-645, doi: 10.1038/ngeo1538.
1049 Wang, J., Z. Jin, R. G. Hilton, F. Zhang, A. L. Densmore, G. Li, and A. J. West (2015a), Controls on
1050 fluvial evacuation of sediment from earthquake-triggered landslides, Geology, 43(2), 115-118,doi:
1051 10.1130/g36157.1.
1052 Wang, J., Z. Jin, R. G. Hilton, F. Zhang, G. Li, A. L. Densmore, D. R. Gröcke, X. Xu, and A. J. West
1053 (2016), Earthquake-triggered increase in biospheric carbon export from a mountain belt, Geology,
1054 44(9), 44(9), doi: 10.1130/g37533.1.
1055 Wang, M., D. Jia, J. H. Shaw, J. Hubbard, A. Plesch, Y. Li, and B. Liu (2014), The 2013 Lushan
1056 earthquake: Implications for seismic hazards posed by the Range Front blind thrust in the Sichuan
1057 Basin, China, Geology, 42(10), 915-918, doi: 10.1130/g35809.1.
1058 Wang, Y., K. Zhang, Q. Gan, W. Zhou, L. Xiong, S. Zhang, and C. Liu (2015b), Bayesian probabilities
1059 of earthquake occurrences in Longmenshan fault system (China), Journal of Seismology, 19(1),
1060 69-82, doi: 10.1007/s10950-014-9451-2.
1061 West, A. J., R. Hetzel, G. Li, Z. Jin, F. Zhang, R. G. Hilton, and A. L. Densmore (2014), Dilution of
1062 ^{10}Be in detrital quartz by earthquake-induced landslides: Implications for determining denudation
1063 rates and potential to provide insights into landslide sediment dynamics, Earth and Planetary Science
1064 Letters, 396(0), 143-153, doi: 10.1016/j.epsl.2014.03.058.
1065 Xu, C., X. Xu, X. Yao, and F. Dai (2014), Three (nearly) complete inventories of landslides triggered
1066 by the May 12, 2008 Wenchuan Mw 7.9 earthquake of China and their spatial distribution statistical
1067 analysis, Landslides, 11(3), 441-461, doi: 10.1007/s10346-013-0404-6.
1068 Xu, C., X. Xu, and J. B. H. Shyu (2015), Database and spatial distribution of landslides triggered by the
1069 Lushan, China Mw 6.6 earthquake of 20 April 2013, Geomorphology, 248, 77-92, doi:
1070 10.1016/j.geomorph.2015.07.002.
1071 Yang, S. L., K. H. Xu, J. D. Milliman, H. F. Yang, and C. S. Wu (2015), Decline of Yangtze River water
1072 and sediment discharge: Impact from natural and anthropogenic changes, Scientific reports, 5, 12581,
1073 doi: 10.1038/srep12581.
1074